Fluid–Thermal–Structural Analysis of Partial Admission Axial Impulse Turbines With Liquid Jet Impingement Cooling

Hanwei Wang
School of Marine Science and Technology,
Northwestern Polytechnical University,
Xi'an, Shaanxi 710072, China
e-mail: wanghanwei@mail.nwpu.edu.cn

Kai Luo
School of Marine Science and Technology,
Northwestern Polytechnical University,
Xi'an, Shaanxi 710072, China
e-mail: nwpu_wyh@nwpu.edu.cn

Ruoyang Zhi
School of Marine Science and Technology,
Northwestern Polytechnical University,
Xi'an, Shaanxi 710072, China
e-mail: zhiruoyang@mail.nwpu.edu.cn

Kan Qin[1]
School of Marine Science and Technology,
Northwestern Polytechnical University,
Xi'an, Shaanxi 710072, China
e-mail: kan.qin@nwpu.edu.cn

Increasing turbine inlet temperature is beneficial to enhance turbine performance. However, this also results in stringent cooling requirements. Unlike turbines in air cycle machines, the partial admission axial impulse turbines for underwater vehicles can utilize the abundant seawater as the cooling medium. In addition, the short blades cannot accommodate the complex cooling channels used in aero-engines, and the alternative way is jet impingement liquid cooling. This paper proposes a fluid–thermal–structural coupling method to investigate the performance of partial admission axial impulse turbines with water-cooling on the rotating wheel front surface. The volume of fluid multiphase model is employed to study the transient gas–liquid interaction, while the Lee model is chosen to model the heat and mass transfer during phase change. Also, a two-way weakly coupling method among fluid, thermal, and structure is utilized to account for fluid–structure interaction. The results show that the temperature distribution at the turbine wheel drops significantly with the jet impingement liquid cooling. The turbine efficiency is also reduced by 3.38% due to the mixing of cooling medium and gas. From stress analysis, the use of water-cooling can minimize turbine damage and ensure stable turbine operation. This study provides insight into the cooling method for partial admission axial impulse turbines for the underwater vehicle. [DOI: 10.1115/1.4063410]

Keywords: liquid jet impingement, multiphase flow, fluid–thermal–structural coupling method, partial admission, phase change, computational fluid dynamics (CFD), fluid dynamics and heat transfer phenomena in compressor and turbine components of gas turbine engines

1 Introduction

Increasing the turbine inlet temperature is an efficient way to enhance output power and thermal efficiency [1,2]. The inlet temperature of the modern gas turbine has reached 1900 K or beyond. This is far higher than the allowable metal temperature [3,4]. Therefore, a suitable cooling strategy must be applied. Various air-cooling strategies, including internal impingement, convection passages, and film cooling, are commonly used in most conventional gas turbines, determined by the application environment and the coolant availability [5].

However, traditional cooling strategies are not appropriate for underwater engines, especially for high-speed applications (over 50 knots). The operating conditions and geometry characteristics of underwater turbines are quite different from the traditional gas turbine. Figure 1 shows a typical turbine and its power system used for underwater vehicles. The underwater power system for this study includes combustor, turbine, and reducer. The fuel contains OTTO-II or OTTO-II, HAP (hydroxylamine perchlorate),

and seawater. The OTTO-II is a mixture of propylene glycol dinitrate, dibutyl sebacate, and 2-nitrodiphenylamine, accounting for 76%, 22.5%, and 1.5% by weight, respectively. Both fuel and combustion products are corrosive; the materials used in underwater systems must be corrosion resistant. The combustor pressure is generally 5–20 MPa. Besides, the thermal efficiency is about 30%, and the output power is around 1 MW. Due to the limited space, high working pressure ratio, and small mass flowrate, the optimal underwater turbines present the characteristics of single-stage, short blade (10–20 mm), partial admission, and impulse type [6]. The rotor diameter is approximately 100–300 mm, and the hub-to-tip ratio is between 0.85 and 0.93. Existing experimental literature [7–9] represented that the total inlet temperature of the underwater turbines is around 1000 K. Kiely and Moore [7] performed a 25.76 mm underwater turbine experiment with an inlet temperature of 1255 K. Small size allowed slow rotor peripheral velocity resulting in lower stress. Therefore, it was possible to work without the cooling structure. Qin et al. provided experiments for 5 kW [8] and 13 kW [9] underwater turbines. The test results involved turbine inlet temperatures from 700 K to 874 K. A cooling structure was not included since the temperature was below the material limit. However, the high rotational speed (50,000–100,000 rpm based on the turbine size) already enabled the rotor to enter the plastic
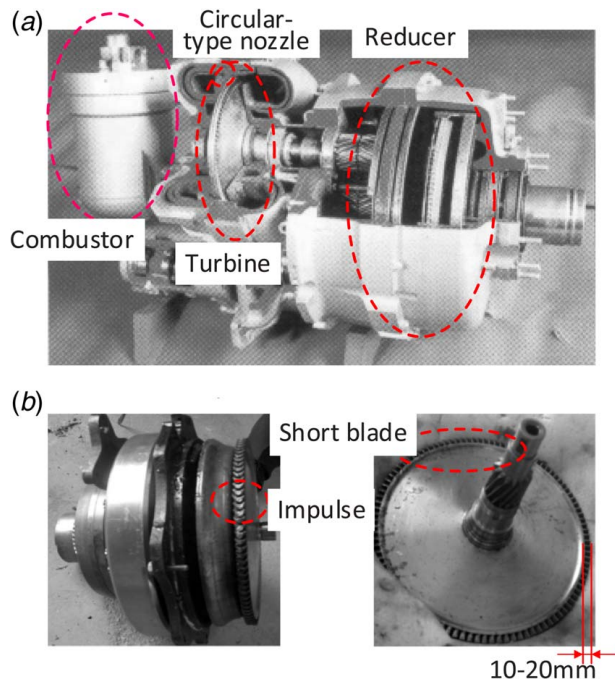
Fig. 1 Turbine used in underwater vehicles: (*a*) power system for underwater vehicle and (*b*) turbine

section, making it hard to accelerate further [10]. Referring to the existing technology, increasing the turbine inlet temperature can improve the operating efficiency, and the operating temperature is highly possible to exceed material temperature permission. It is difficult to obtain an amount of cooling gas due to the lack of air in the underwater environment. Therefore, liquid water-cooling is preferred considering the abundant seawater.

The liquid cooling techniques have been considered in turbines since the 1900s to enable higher temperature operation [11]. After decades of development, the potential for liquid cooling was indicated in the review [12,13]. It was pointed out that the ultimate potentialities of liquid cooling were higher than that of the corresponding air-cooled system regarding maximum allowable gas temperature, cycle efficiency, and specific output. Generally, like air cooling, liquid cooling can be divided into two forms—external cooling (such as air/water mist cooling, spray cooling, and sweat cooling) and internal cooling (such as air/water mist cooling, forced-convection cooling, and free-convection cooling). Existing cooling schemes can basically ensure the stability of the water-cooled turbine operation. However, the complex structure and small flow path of the impeller and blade may lead to plugging. In addition, regarding thermal efficiency, the mass flowrate of the water needs to be maintained at a low level, which is prone to liquid depletion and causes a rapid increase in local temperature. Therefore, with the rise of air-cooled technology, liquid cooling seems gradually fading out of the research field after the 1980s. Nevertheless, further research is needed for the high-speed underwater application, which can only consider water-cooling. Table 1 summarizes the literature on turbine liquid cooling methods after the 1980s.

In the early 1980s, some researchers still carried out high-temperature experiments and simulation methods for blade internal cooling with water-cooling. Horner et al. [14] presented an experimental investigation of the turbine used in the Integrated Gasification Combined Cycle. The results indicated that the firing temperature could reach 1922 K (nozzle inlet temperature 1755 K) for a properly designed water-cooled turbine. Schilke and DeGeorge [15] fabricated and tested a second-stage water-cooled nozzle in a combined cycle. Amano [16] provided a numerical method to predict the flow and heat transfer around the blade using internal water-cooling.
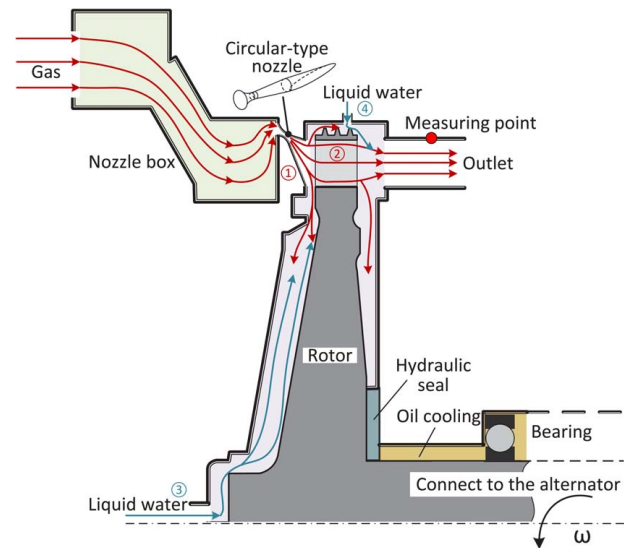
Since then, this approach has been used mainly as a cooling source for some theoretical research experiments. Ladisch et al. [17] carried out a heat transfer experiment on a highly loaded low-pressure airfoil using ten water-cooling holes. And then, Duchaine

Table 1 Summary of the turbine with liquid cooling after the 1980s

Author	Year	Study type	Cooling form	Liquid coolant	Gas temperature
Horner et al. [14]	1981	Experimental	Internal cooling	Water	1755 K/1411 K
Schilke and DeGeorge [15]	1982	Experimental	Internal cooling—125 cooling holes	Water	1200 K–1412 K
Amano [16]	1982	Numerical	Internal cooling	Water	1473 K
Nirmalan et al. [24]	1998	Experimental	External & internal cooling—mist film cooling	Air/water mist	811 K/950 K/1089 K
Elhabeshi and Guo [20]	2005	Experimental and numerical	Internal cooling—closed-loop and thermosyphon cooling	Water	Hot gas provides 313 K (EXP)/373 K (CFD) wall temperature
Townsend et al. [21]	2008	Experimental	Internal cooling—RFC technology thermosyphon	Potassium	Resistance-heated
Ladisch et al. [17]	2009	Experimental	Internal cooling—ten cylindrical cooling channels	Water	350 K (tot)
Lorenz et al. [19]	2011	Experimental	Internal cooling—eight cylindrical cooling channels	Water	350 K (tot)
Duchaine et al. [18]	2013	Numerical	Internal cooling—ten cylindrical cooling channels	Water	348 K (tot)
Ragab and Wang [25,26]	2018	Experimental	External cooling—mist film cooling	Air/water mist	327 K
Wang et al. [27,28]	2019, 2021	Numerical	External & internal cooling—mist film cooling	Air/water mist	600 K 1708 K (tot)
Lytvynenko et al. [22]	2020	Numerical	Internal cooling—porous medium filled liquid metal	Natrium	1373 K
Zhang et al. [23]	2021	Numerical	Internal cooling—U-shaped channel	Gallium-indium alloy/air	818 K (tot)
Abdelmaksoud et al. [29,30]	2021, 2022	Experimental and numerical	External & internal cooling—mist film cooling	Air/water mist	328 K/1645 K
Cao et al. [31]	2022	Experimental	Internal cooling—mist film cooling	Air/water mist	880 K

et al. [18] focused on conjugate heat transfer analysis based on the large-eddy simulation through the results of the previous experiment [17]. Lorenz et al. [19] also used internal water-cooling to analyze a heat transfer experiment of the highly loaded low-pressure blade with different surface roughness.

The main focus of the current internal cooling study has shifted to the thermosyphon using water or liquid metals. Elhabeshi and Guo [20] reported a closed-loop thermosyphon rotor using liquid water to prevent additional mainstream mixing losses caused by film cooling. Townsend et al. [21] developed a return-flow cascade thermosyphon potassium cooling method to obtain near-uniform blade temperature distribution. Lytvynenko et al. [22] presented a cooling method using a porous medium filled with a two-phase liquid coolant. They proposed a numerical solution to solve the thermal conductivity of this multilayer system. A numerical analysis using liquid metal (Gallium-indium alloy) was also carried out by Zhang et al. [23]. They compared the heat transfer effects between the air and liquid metal with a forced convective U-shaped channel.

Mist film cooling combines the advantages of gas film cooling and liquid cooling, which is an extension of existing technologies. Nirmalan et al. [24] found that the cooling air could reduce by more than 50% using the water–air cooling technique by presenting an experimental study of a mist film cooling airfoil. Ragab and Wang investigated heat transfer [25] and two-phase droplet multiphase flow [26] of the mist/air film cooling through wind tunnel experiments using a flat plate of fan-shaped holes. Wang and Ragab [27] conducted a numerical study to ensure the possibility of the transport of mist water to the rotating blades. Wang and Abdelmaksoud [28] simulated a transonic turbine stage using a 2D two-phase numerical method to study the air–water mist cooling effect on wakes and shock waves. Abdelmaksoud and Wang. [29] then extended the previous numerical method to a 3D vane combined with internal and external cooling. Abdelmaksoud et al. [30] further carried out an experiment on a wind tunnel system, and then the experimental results were used to validate and improve the numerical method. Cao et al. [31] pointed out that mist/air cooling with a mass ratio of 3% can improve cooling performance significantly by studying the mist/air heat transfer performance in a high-temperature channel experiment.

However, the existing turbine liquid cooling technologies are often accompanied by complex internal structures. Due to the small size of the blade, the dimension of the internal cooling structure is correspondingly reduced, and the machining difficulty rises significantly. In addition, the wheel and blades are typically machined together for underwater turbines to ensure blade strength at high rotational speeds. Thus, the existing cooling strategy cannot be used for underwater vehicles. Figure 2 illustrates some feasible liquid jet impingement cooling strategies for underwater turbines. These methods use external cooling to avoid creating internal cooling paths in the rotor. One possible way is to inject into the turbine from the center of the front clearance to reduce the rotor temperature (Fig. 2 point 3). The other feasible approach is to inject liquid from the tip clearance (Fig. 2 point 4) to directly cool the blades. The former cooling method is the focus of this paper. The turbine with the water-cooling includes complex multiphase flow phenomena coupled with multiphysics. Existing datasets [32,33] lack some thermodynamic parameters of seawater. In addition, the difference between pure water and seawater (ocean salinity 35 g/kg) is not large under the available data range. Therefore, this study uses pure water as the coolant. This paper aims to provide a multiphase fluid–thermal–structure coupling method to study the flow and heat transfer characteristics, stress distribution, and turbine performance for this particular application.

The remainder of this paper is organized as follows. Section 2 introduces the fluid–thermal–structural coupling method. Three test cases are then selected as the model validation in Sec. 3. Section 4 demonstrates the flow, temperature, stress, and deformation analysis of the turbine with liquid jet impingement cooling.

Fig. 2 Schematic of the turbine using jet impingement liquid cooling: (1) circular-type nozzle, (2) turbine blades, (3) cooling position at axial direction, and (4) cooling position at radial direction

2 Methodologies

2.1 Computational Method. Partial admission turbine with liquid cooling involves complex mass and heat transfer characteristics. In addition, the heat and mass transfer between liquid water and high-speed hot gas is essential. Moreover, the flow characteristics and temperature distribution are significantly different due to the partial admission structure. The significant temperature difference before and after water-cooling affects the rotor deformation, directly changing the tip clearance and turbine efficiency. Therefore, the wheel temperature and deformation are also necessary to be investigated to provide the accurate turbine performance prediction.

To accurately simulate the complicated flow phenomena, the volume of fluid (VOF) method is utilized to model the interaction between incompressible liquid water and compressible mixture fluid (vapor and gas). The species transport equation is used for modeling the diffusion within the mixture. The governing equations are the following:

Continuity equation for the mixing of liquid water and compressible mixture fluid

$$\frac{\partial(\rho_{\mathrm{m}})}{\partial t} + \nabla \cdot (\rho_{\mathrm{m}}\mathbf{v}) = 0 \tag{1}$$

Continuity equation for the liquid water

$$\frac{\partial(\alpha_{\mathrm{l}}\rho_{\mathrm{l}})}{\partial t} + \nabla \cdot (\alpha_{\mathrm{l}}\rho_{\mathrm{l}}\mathbf{v}) = S_{\mathrm{l}} \tag{2}$$

Continuity equation for the compressible mixture fluid using species transport equation

$$\frac{\partial(\alpha_{\mathrm{mf}}\rho_{\mathrm{mf}}Y_i)}{\partial t} + \nabla \cdot (\alpha_{\mathrm{mf}}\rho_{\mathrm{mf}}\mathbf{v}Y_i) = -\nabla \cdot \mathbf{J}_i + S_{\mathrm{mf}} \tag{3}$$

Momentum equation

$$\frac{\partial(\rho_{\mathrm{m}}\mathbf{v})}{\partial t} + \nabla \cdot (\rho_{\mathrm{m}}\mathbf{v}\mathbf{v}) = -\nabla p + \nabla \cdot (\bar{\bar{\tau}}) \tag{4}$$

Energy equation

$$\frac{\partial(\rho_{\mathrm{m}}E)}{\partial t} + \nabla \cdot (\mathbf{v}(\rho_{\mathrm{m}}E + p)) = \nabla \cdot \left(k_{\mathrm{eff}}\nabla T - \sum_i h_i \mathbf{J}_i + \bar{\bar{\tau}}_{\mathrm{eff}} \cdot \mathbf{v}\right) + S_{\mathrm{h}} \tag{5}$$

The viscous heating effect is also applied in the energy equation. The ANSYS FLUENT solver [34] with SIMPLEC algorithm is used to solve steady-state and transient-state simulations, respectively. Due to the effect of multiphase and rotation, the steady-state with multiple moving reference frame method will significantly deviate from the actual situation. The rotor is frozen during steady-state calculations, and the liquid water moves along the direction of relative velocity. Since the velocity of liquid water is without a circumferential component, a reverse relative velocity is imposed when entering the rotor domain, which results in a significant mass fraction difference. Therefore, the transient-state calculation with dynamic mesh motion is utilized, while the steady-state calculation provides a suitable initial condition. The Realizable $k - \varepsilon$ turbulence model with the scalable wall function is used to close Reynolds-averaged Navier–Stokes equations.

$$\frac{\partial}{\partial t}(\rho_{\mathrm{m}} k) + \nabla \cdot (\rho_{\mathrm{m}} k \mathbf{v}) = \nabla \cdot \left[\left(\mu_{\mathrm{m}} + \frac{\mu_{\mathrm{t}}}{\sigma_k}\right)\nabla k\right] + G_k \quad (6)$$

$$\frac{\partial}{\partial t}(\rho_{\mathrm{m}} \varepsilon) + \nabla \cdot (\rho_{\mathrm{m}} \varepsilon \mathbf{v}) = \nabla \cdot \left[\left(\mu_{\mathrm{m}} + \frac{\mu_{\mathrm{t}}}{\sigma_\varepsilon}\right)\nabla \varepsilon\right] + \rho_{\mathrm{m}} C_1 S \varepsilon$$
$$- \rho_{\mathrm{m}} C_2 \frac{\varepsilon}{k + \sqrt{\nu_{\mathrm{m}} \varepsilon}} \quad (7)$$

The second-order upwind is applied for spatial discretization. Besides, the warped-face gradient correction is adopted to improve numerical convergence. In addition, the Lee model is selected to compute the boiling rate by the user-defined function. The mass transfer and the energy change are added to the continuity and energy equations by adding source terms, respectively. The mass source in the continuity equation is computed as

$$S_{\mathrm{l}} = -S_{\mathrm{mf}} \quad (8)$$

$$\begin{cases} S_{\mathrm{mf}} = c_{\mathrm{lv}} \alpha_{\mathrm{w}} \rho_{\mathrm{w}} \dfrac{T - T_{\mathrm{sat}}}{T_{\mathrm{sat}}} & T > T_{\mathrm{sat}} \\[2mm] S_{\mathrm{l}} = c_{\mathrm{vl}} \alpha_{\mathrm{mf}} \rho_{\mathrm{v}} \dfrac{T_{\mathrm{sat}} - T}{T_{\mathrm{sat}}} & T < T_{\mathrm{sat}} \end{cases} \quad (9)$$

The boiling saturation temperature for each cell is obtained from the Antoine equation [35] with T_{sat} in K and P in Pa, which is

$$T_{\mathrm{sat}} = 45.47 + \frac{3826.36}{9.3876 - \ln\left(\frac{p}{1e^6}\right)} \quad (10)$$

The mass transfer results in energy change, and the heat source for the energy equation is

$$S_{\mathrm{h}} = S_{\mathrm{l}} h_{\mathrm{l}} = -S_{\mathrm{mf}} h_{\mathrm{l}} \quad (11)$$

The latent heat with a quadratic function is interpolated from the REFPROP database [36]. The equation is calculated with T_{sat} in K and h_{l} in J/kg.

$$h_{\mathrm{l}} = -14.86 T_{\mathrm{sat}}^2 + 10250 T_{\mathrm{sat}} + 417400 \quad (12)$$

For the solid domain, the steady-state thermal conduction is also solved in FLUENT software. The ANSYS Mechanical APDL [34] with preconditioned conjugate gradient (PCG) solver is used for the steady-state nonlinear strength calculation. The steady-state energy transport equation can be expressed as

$$\nabla \cdot (k_T \nabla T) = 0 \quad (13)$$

The steady-state equilibrium equation is

$$\nabla \cdot \sigma + F = 0 \quad (14)$$

Based on the test data at different temperature conditions, the material properties are assumed to depend on the temperature change. In addition, the bilinear isotropic hardening plasticity is

also considered, and the full Newton-Raphson method is used to solve nonlinear equations during iteration.

2.2 Coupling Procedure. The fluid and thermal simulations are strongly coupled in the same solver, while the structure simulation is weakly coupled in the different solvers. Therefore, to deal with the data transfer between different simulations, a fluid–thermal–structure coupling method for partial admission axial turbines is established in Fig. 3. The whole simulation procedure is as follows:

(1) Establish the initial computational domain.
(2) The fluid domain with the initial wall temperature $T_{\mathrm{w,f}}^k$ at the fluid–thermal interface is solved until convergency for both steady-state and transient-state simulations. The steady-state result is used as the initial value for the transient-state simulation. For the transient simulation, the implicit transient formulation is used for the time-advancement algorithm, which allows a relatively high Courant number and reduces the computational expense [37]. Generally, Courant numbers less than 10 can achieve accurate results [38]. In this paper, the average Courant number is approximately 7. The convergence criterion of steady-state simulation is based on that the difference in total-to-static efficiency is less than 10^{-3} between two consecutive steps. For transient simulations, the convergence is obtained when the difference in time-averaged total-to-static efficiency is less than 10^{-3} between two consecutive cycles.

$$\eta_{\mathrm{ts}} = \frac{P_{\mathrm{output}}}{P_{\mathrm{available}}} = \frac{M \cdot \omega}{\dot{m}_{\mathrm{gas}} \cdot \Delta h_{\mathrm{is}}} \quad (15)$$

(3) The heat flux q and near-wall temperature T_{nearwall} at the fluid–solid interfaces are extracted from the fluid domain. T_{nearwall} is the local fluid temperature adjacent to the wall at the first layer of the mesh.
(4) The heat flux is then transferred from the fluid domain to the solid domain. The time-averaged value is used for the calculation. The convective heat transfer coefficient h is then calculated as

$$h = \frac{q}{T_{\mathrm{nearwall}} - T_{\mathrm{w,f}}^k} \quad (16)$$

(5) The convective heat transfer coefficient h and the near-wall temperature T_{nearwall} are then taken as the boundary conditions for the thermal simulation. The temperature distribution in the solid domain is solved until the solution is converged. The convergence criterion is that the energy residual is lower than 10^{-11}.
(6) The wall temperature $T_{\mathrm{w,s}}^k$ at the interfaces from the thermal simulation is extracted. The new wall temperature $T_{\mathrm{w,f}}^{k+1}$ as the boundary condition for fluid simulation is then used (Eq. (17)). The under-relaxation factor β is initially set as 0.1 and then changed to 0.3 for acceleration.

$$T_{\mathrm{w,f}}^{k+1} = T_{\mathrm{w,f}}^k + \beta(T_{\mathrm{w,s}}^k - T_{\mathrm{w,f}}^k) \quad (17)$$

(7) Repeat steps 2–6 using the updated $T_{\mathrm{w,f}}^{k+1}$ until convergence. Typically, a converged solution needs 30–40 iteration loops. The convergence criterion is that the maximum relative difference of the wall temperature is less than 10^{-3} between two consecutive iteration loops.
(8) The temperature at the solid domain T_{s} and time-averaged wall pressure at fluid domain $p_{\mathrm{w,m}}$ and rotational speed ω are then mapped to the structural simulation. The profile-preserving transfer is applied to control the accuracy during data mapping. In addition, the bucket surface search algorithm is used to locate a source element that
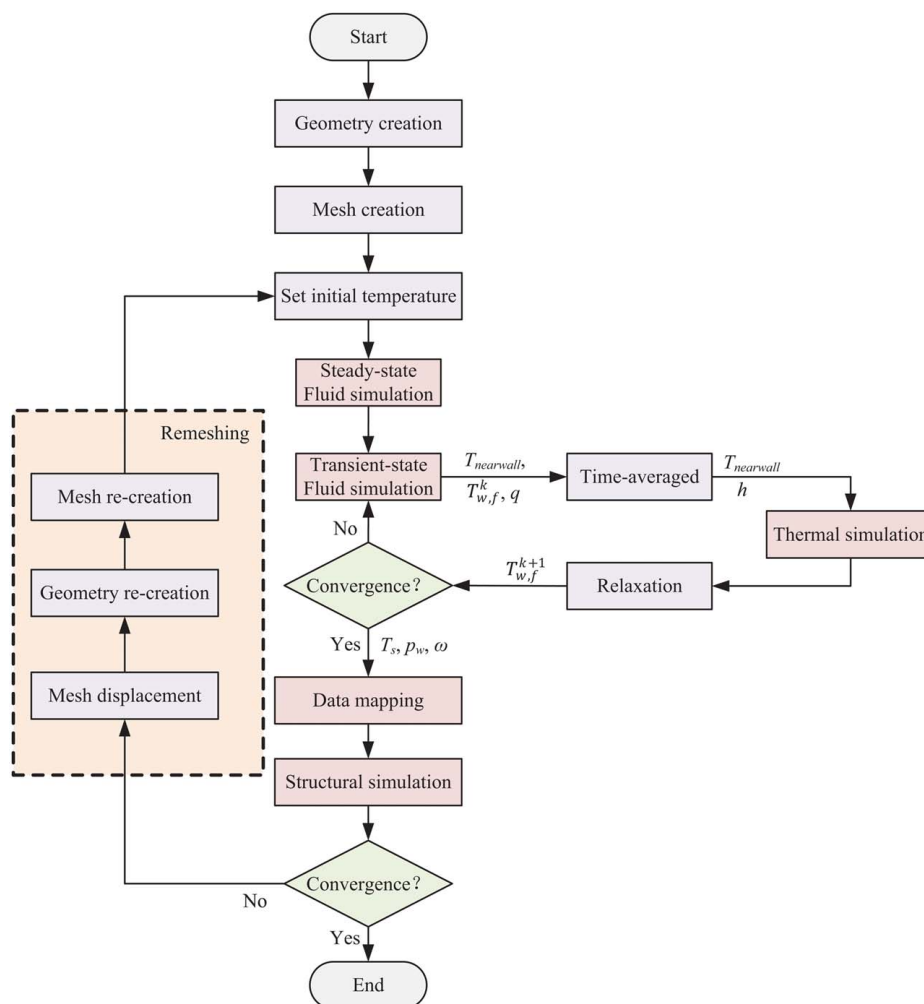
Fig. 3 Coupling procedure for fluid–thermal–structural simulation

each target node can be mapped. The triangulation method is selected as the weighting type.

(9) The mesh displacement in the solid domain is solved until the structure simulation is converged. The convergence tolerance of the PCG solver is 10^{-8}.

(10) The new geometry and mesh are then updated. The skin detection algorithm scans the exterior element facets and groups them based on a tolerance angle. The faces are then formed, and the geometry is created by sewing. The topology is then re-associated based on the new model, and the hexahedral mesh is generated.

(11) Repeat steps 2–10 using the updated mesh until convergence. It typically needs about 2–3 iteration loops. The

convergence criterion is that the maximum relative difference of total displacement is less than 10^{-2} between two consecutive iteration loops.

3 Model Validation

The model validation is performed in this section to test the suitability of the proposed computational approach. A test case predicting the experimental wall temperature of a cooled nozzle validates numerical conjugate heat transfer results. Then, the experiment regarding supersonic gas and water-cooling is used to validate the suitability of the mixing problem between the two phases. The last one provides liquid jet impingement cooling experimental
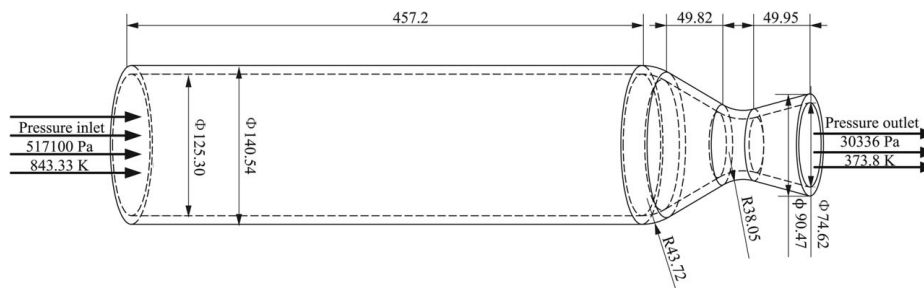
Fig. 4 Geometry and operating condition for the experiment nozzle

results of the high-temperature turbine, validating the reliability of the numerical method.

3.1 Conjugate Nozzle Flow.

The first case is from the experiment of a cooled axisymmetric convergent–divergent nozzle [39].
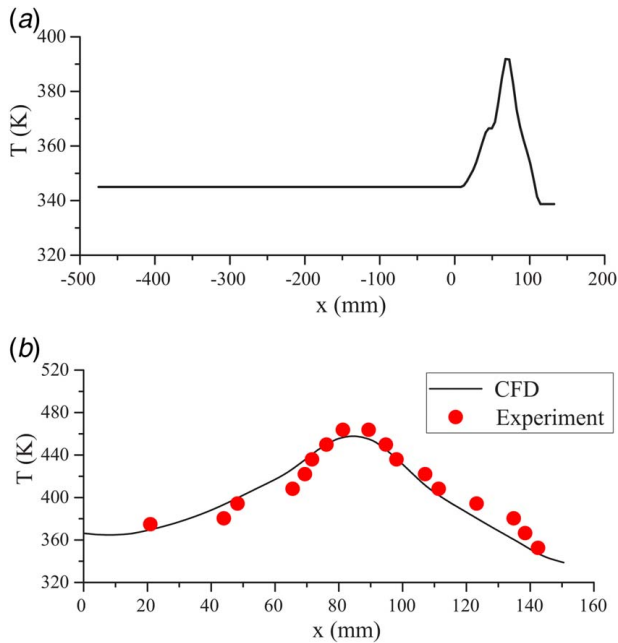
Fig. 5 The input outer wall temperature and output inner wall temperature result for the experiment nozzle: (a) input and (b) result

The geometry and operation conditions obtained from DeLise and Naraghi [40] are shown in Fig. 4. The nozzle has a stable section of 457.2 mm and a measurement section with an inner diameter ratio of 2.74:1:1.63 at the inlet, throat, and outlet. The throat diameter is 45.8 mm, and the half angle of the convergent and divergent is 30 deg and 15 deg, respectively. The thickness of the solid domain is 7.62 mm. The nozzle inlet is set as total pressure and total temperature, while static pressure is for the outlet. The material property of thermal conductivity is 27 W/(m · K), referring to Marineau et al. [41]. The outer wall is water-cooled, and a nonuniform temperature distribution obtained from the experiment is used for the boundary conditions (Fig. 5(a)). The comparison between numerical results and experimental data is shown in Fig. 5(b). It is shown that the predicted wall temperatures are close to the experimental values. The result also confirms that the proposed fluid–thermal method is able to predict the solid temperature distribution.

3.2 Supersonic gas Cooling With Liquid Water.

The experimental results from Yi et al. [42] for solid rocket motor are carried out to test the numerical model for mixing high-temperature gas and liquid water. The schematic of the computational domain is shown in Fig. 6(a). The distance from the nozzle to the launch ground wall is 1.75 m, and the spacing between the two test points on the target wall is 0.1 m. Four water pipes are equally distributed around the nozzle, and the angle between the pipes and the axis is 60 deg. A quarter of the 3D computation domain is used in this simulation with symmetry boundary conditions (see Fig. 6(b)).

The total pressure and temperature inlet of 7 MPa and 3000 K are set at the nozzle inlet, while 1 atm static outlet is set around the domain (see Fig. 6). Besides, the velocity inlet at the water pipes is 25 m/s for the four-pipe case and 16 m/s for the two-pipe case. The two-pipe case presents clear experimental results [43]; this can be used to verify the suitability of the VOF model. The
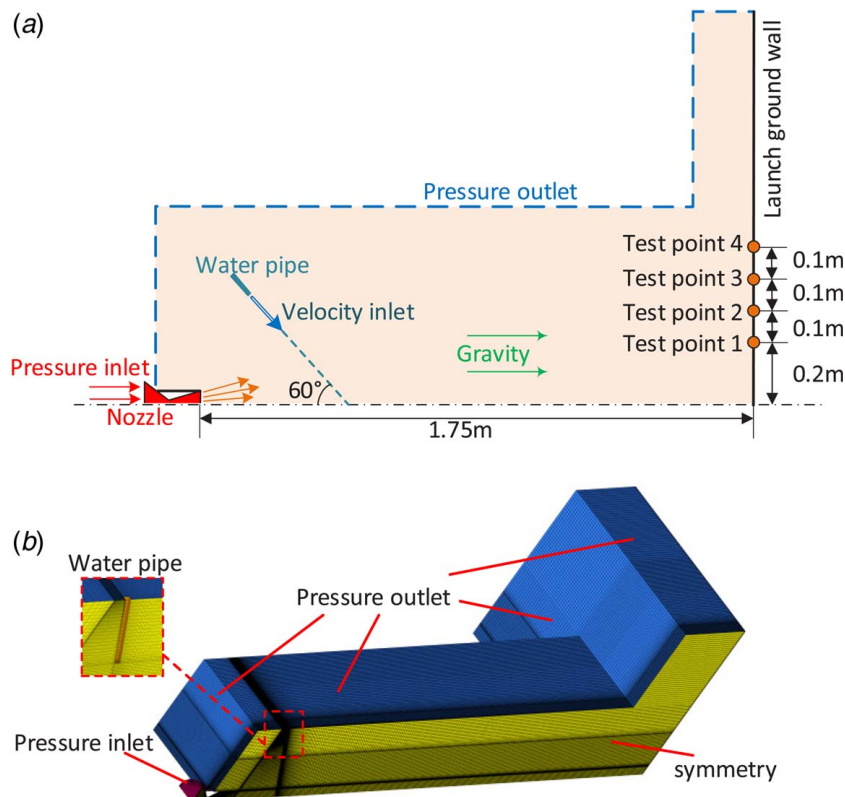

Fig. 6 Schematic of the supersonic gas cooling experiment: (a) schematic of the boundary conditions and (b) computation domain

gravity of 9.8 m/s² is also considered in this study. Five species (H₂O, CO, H₂, CO₂, and N₂ with the mass fractions of 0.16, 0.27, 0.004, 0.26, and 0.306) are applied, while the combustions among species are ignored. In addition, the temperature at the water inlet and pressure outlet is 300 K. The walls are set as no slip and adiabatic. The test results of the two-pipe case are influenced by the environment at the bottom [43]. The velocity near the nozzle outlet is high and slightly affected by the environment, while the temperature results are influenced by the boundary. The water and vapor distribution is used to verify the suitability of VOF. As shown in Fig. 7, the computational fluid dynamics (CFD) distribution of water and vapor is close to the experimental result. The comparison of test point temperature between the experiment of the four-pipe case and CFD results is shown in Table 2. The maximum relative difference is 10.2%, confirming that the numerical model can predict the mixing problems between high-temperature gas and liquid water.

3.3 High-Temperature Gas Turbine Using Liquid Jet Impingement Cooling.

To further validate the proposed numerical method, an experimental facility is established. A shrouded partial admission impulse turbine is designed and machined (see Fig. 2). Table 3 shows the corresponding geometric parameters. The main components also include the pump, combustor (propellant: OTTO-II, HAP, and water), condenser, and other auxiliary components (see Fig. 8). The high-temperature and high-pressure gas is first produced in the combustor. The combustion temperature is controlled by the water percentage. The thermal energy is then converted into supersonic flow through the nozzle (Fig. 2 point 1), and the high-speed gas impinges on the turbine blades (Fig. 2 point 2) to produce mechanical energy.

Meanwhile, cooling water is injected from the axial (Fig. 2 point 3) and radial (Fig. 2 point 4) direction of the turbine to reduce the wheel temperature. The high-temperature gas and water (containing liquid and vapor) mix and discharge through the outlet. Besides, the output power is attained by the voltage and the impedance load, which is transferred from the alternator connected to the turbine.
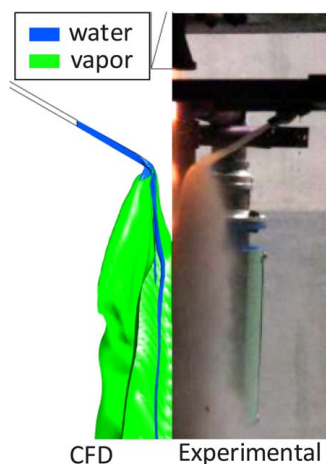

Fig. 7 Comparison of CFD and experimental results

Table 2 Comparison of experiment and numerical results for supersonic gas cooling

	Test point	1	2	3	4
Without water	Experiment	1000 K	940 K	830 K	681 K
	CFD	917.25K	844.53 K	781.88 K	725.82 K
With water (four-pipe)	Experiment	422 K	415 K	410 K	402 K
	CFD	400.48 K	392.27 K	385.78 K	381.89 K

Table 3 Geometric parameters for partial admission axial impulse turbine

Parameters	Value
Nozzle number	4
Nozzle throat diameter	4.9 mm
Nozzle outlet diameter	9.0 mm
Nozzle angle	13 deg
Partial admission ratio	0.33
Rotor number	75
Blade median diameter	175 mm
Rotor blade angle	25 deg
Hub-to-tip ratio	0.88

The thermocouples and pressure transducers are installed at the inlet and outlet to obtain the boundary conditions and validation data for numerical calculation.

The operating conditions are listed in Table 4. Three working conditions are carried out in this experiment. The maximum operation condition is Exp 1, which is also the baseline for the others. The output power and the outlet temperature are measured as a reference to verify the accuracy of the numerical model. The numerical and experimental results are summarized in Table 5, and the maximum relative difference is 10.8% and 4.7% for the output power and the measuring point temperature, respectively. The results further confirm that the proposed numerical method can be adopted for the performance prediction of water-cooling turbines.

4 Results and Discussion

4.1 Boundary Conditions and Independence Test.

In this section, the detailed fluid–thermal–structural simulation of the water-cooling turbine is described. The axial liquid water
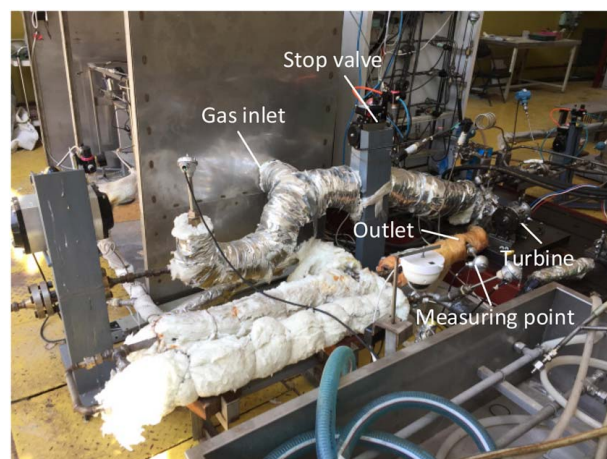

Fig. 8 Experimental facility for the test turbine

Table 4 Operating conditions for the experiment

Parameters	Exp 1	Exp 2	Exp 3
Nozzle inlet total pressure	1	0.417	0.542
Nozzle inlet total temperature	1	1.038	0.962
Outlet static pressure	1	0.692	0.692
Rotational speed	1	0.5	0.6
Mass flowrate of axial direction liquid water	1	0.75	0.85
Temperature of axial direction liquid water	1	1	1
Mass flowrate of radial direction liquid water	1	1	1
Temperature of radial direction liquid water	1	1	1

**Table 5 Comparison of the numerical and experimental results for test turbine**

Parameters	Output power	Measuring point temperature
Exp 1	1	1
CFD 1	1.005	1.047
Exp 2	0.233	0.776
CFD 2	0.248	0.790
Exp 3	0.417	0.768
CFD 3	0.462	0.737

impingement cooling toward the center of the wheel is investigated in this paper (Fig. 2 point 3). The computational model is from the test turbine mentioned in Sec. 3.3. The working condition of the design point is selected (Exp 1 in Sec. 3.3), and the boundary conditions are listed in Table 6. For the fluid domain, the nozzle inlet is set as the total pressure and temperature (19 MPa and 1373 K), while the static pressure is defined as the outlet boundary condition. The mass flowrate of 0.2 kg/s is adopted at the water inlet. The mesh motion with a shaft speed of 50,000 rpm is set on the rotor domain. The rotor walls (including the blade, wheel, and shroud) are modeled as the fluid–solid interface, while other walls are assumed to be adiabatic. For the solid domain, the rotor walls connected to the fluid domain are the fluid–solid interface. The material properties are modeled as temperature dependent, and the yield and fracture strength are shown in Fig. 9. A hydraulic seal is installed at the shaft root on the back side of the rotor (Fig. 2), and a large amount of cooling water is required for sealing and cooling. Lubricating oil also fills the bearing. Therefore, a fixed temperature boundary condition is adopted, and the value is determined by the temperature of cooling water and oil. The fixed support constraint is applied to the shaft end surface aligning with the bearing support point.

The mesh independence is then tested by using the nondimensional total-to-static efficiency. The assembly model is used for the mesh independence check. The nozzle box is not considered in the simulation model since the velocity in the nozzle box is very small. To provide sufficient data transfer accuracy, the fluid

Table 6 Boundary conditions

Location	Boundary conditions
Fluid domain	
Nozzle inlet	Total pressure 19 MPa
	Total temperature 1373 K
Outlet domain outlet	Static pressure 0.5 MPa
Rotor domain	Rotational sliding mesh, 50,000 rpm
Nozzle domain	Stationary
Outlet domain	Stationary
Interface between fluid domain	Nonconformal interfaces
Rotor walls	Coupling wall
Other walls (turbine casing)	Adiabatic, no slip
Fluid	Ideal gas mixing for mixed fluid
	Incompressible for water liquid
Water inlet	Mass flow inlet 0.2 kg/s
	Temperature 328.15 K
Solid domain	
Shaft cooling temperature	340.65 K
Shaft end surface	Fixed support
Rotor walls	Coupling wall
Material	
Density	8.2 g/cm^3
Young's modulus	$-0.0584\,T + 232.6$ GPa
Poisson ratio	~0.4
Thermal expansion coefficient	$(0.0056\,T + 8.6763) \times 10^{-6}$ °C
Thermal conductivity coefficient	$0.0108\,T + 5.7129$ W/m·K
Yield strength	Fig. 9 solid line
Fracture strength	Fig. 9 dashed line
Elongation	$0.01 \times e^{0.007 \times T} + 7.98$ percentage
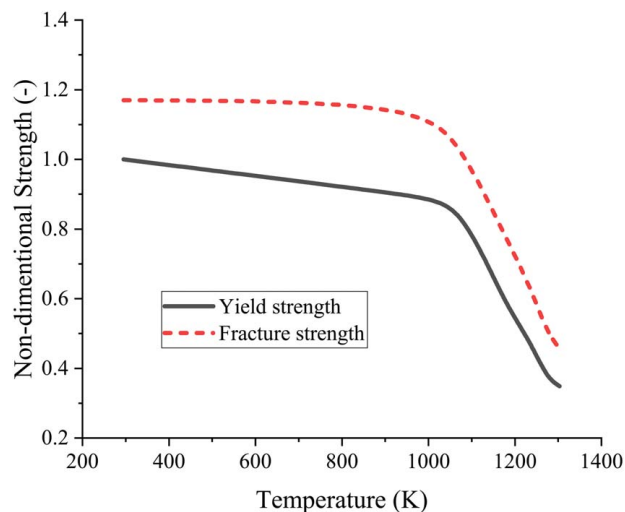
Fig. 9 Variation of yield strength and fracture strength with temperature for K418-modify

and solid domains must be simultaneously topologized to keep the nodes matched at the coupling interface. In addition, the entire fluid domain is modeled due to the partial admission asymmetrical geometry. Compared to the solid thermal simulation, the fluid simulation is more difficult to converge. Therefore, the convergence of fluid calculation is used as the judgment, while the solid mesh can be obtained according to fluid node distributions. As shown in Table 7, the total node number for the fluid domain of about 13 million is found to be suitable for predicting the performance. Figures 10(a)–10(c) show the selected computational mesh.

The independence of time-step and subiterations is also tested. The time-step should be selected to ensure the blades can return to the initial position after one cycle to facilitate data transfer. As the results are shown in Tables 8 and 9, the accuracy of the time-step of 3.2 μs and the subinteractions of 20 is sufficient to ensure convergence. The relative difference in the efficiency the between selected and lowest Courant number is 0.7%. To provide more detail, the Courant numbers effect for the moment of the monitored blade in one cycle is also tested. As shown in Fig. 11, Courant number 7 can capture the moment variation well. The subcycles for the fluid–thermal coupling are then tested by the nondimensional near-wall temperature (see Table 10). Five cycles are acceptable in this study regarding computational costs. In addition, the mesh independence of the structural calculation is also tested using the nondimensional maximum Von Mises stress and deformation. The calculation process is loaded with centrifugal force. The node number of the solid domain for stress calculation at 1 million can satisfy the calculation requirements (Table 11), and the selected mesh is shown in Fig. 10(d).

4.2 Flow and Heat Transfer Characteristics. This section describes the turbine performance, flow, and heat transfer characteristics. Table 12 illustrates the effect of the deformation on turbine performance. The turbine efficiency of water-cooling is 50.76%,

Table 7 Variation of nondimensional efficiency by nodes number

Nodes number for fluid domain/million	Nondimensional efficiency
4	0.910
9	0.989
13	**1**
17	1.003

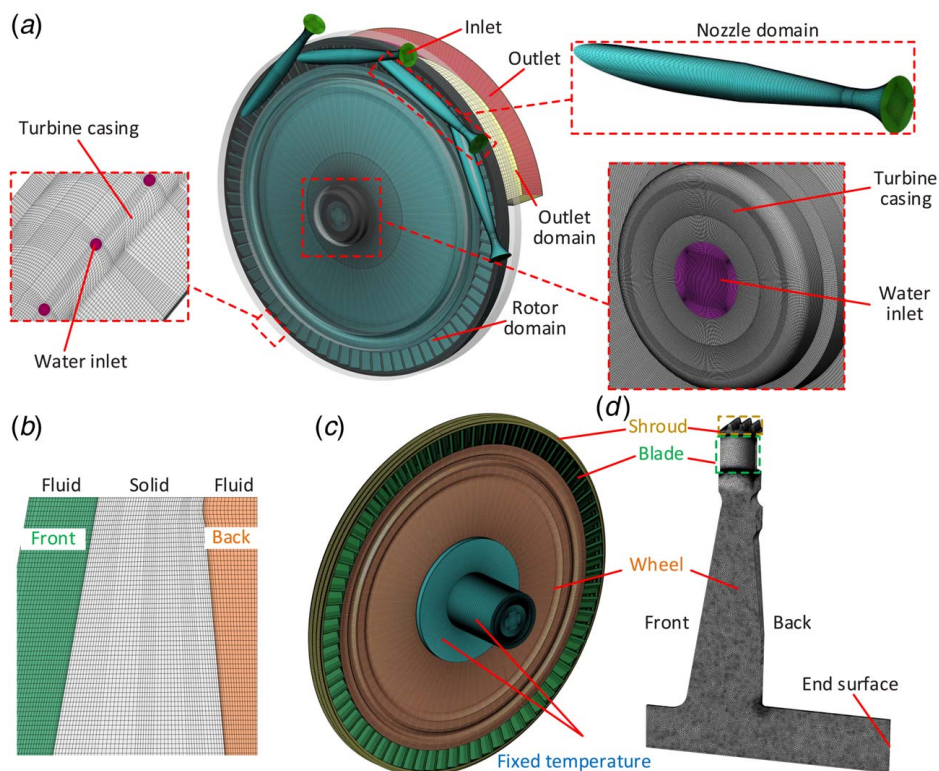Note: Bold value indicates selected nodes number for fluid simulation.

Fig. 10 Computational domain and mesh configuration of the water-cooling turbine: (*a*) fluid domain, (*b*) nodes matching, (*c*) solid domain for thermal simulation, and (*d*) solid domain for stress simulation

Table 8 Variation of nondimensional efficiency by time-step

Time-step size/μs	Period/ nozzle	Period/ rotor	Nondimensional efficiency	Courant number
8	12	2	0.952	17.5
5	19.2	3.2	0.987	11
3.2	**30**	**5**	**1**	**7**
2	48	8	1.005	4.4
0.4	240	40	1.007	0.88

Note: Bold value indicates selected time-step.

Table 9 Variation of nondimensional efficiency by subiterations for time-step

Subiterations for time-step	Nondimensional efficiency
10	0.912
20	**1**
30	0.998

Note: Bold value indicates selected subiterations.

decreasing by 3.38% compared with non-water-cooling (54.14%). Therefore, if the rotor does not fail, liquid cooling is not recommended. However, liquid cooling is recommended if the rotor is fractured, such as the turbine in this study. Besides, the difference between deformation and original geometry is significant. Without water-cooling, a relative difference of 10.75% in the total-to-static efficiency is found, while the water-cooling case also has a relative difference of 10.22%. Therefore, the deformation in the partial admission turbine must be accurately obtained using the fluid–thermal–structural coupling method. To intuitively provide the influence of water-cooling at the blade inlet and outlet, Fig. 12 shows the area-averaged velocity triangle in the working section. The absolute velocity (water-cooling: 1327.9 m/
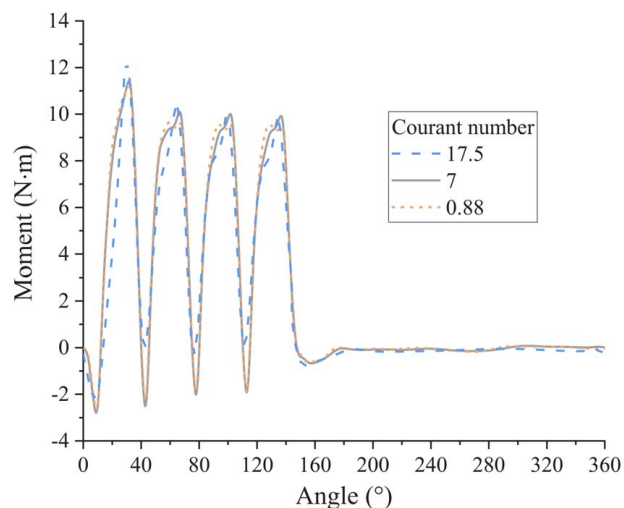

Fig. 11 Courant number effect for the blade moment within one cycle

Table 10 Variation of nondimensional near-wall temperature by subcycles for each coupling

	Nondimensional averaged near-wall temperature			
Subcycles	Front	Back	Clearance	Rotor
1	0.9887	0.9931	0.9923	0.9710
2	0.9929	0.9969	1.0070	0.9803
3	0.9971	0.9990	0.9977	0.9956
4	0.9986	0.9996	1.0040	0.9984
5	**1**	**1**	**1**	**1**
6	1.0011	1.0003	1.0015	1.0013

Note: Bold value indicate selected subcycles.

Table 11 Variation of nondimensional maximum Von Mises stress and deformation by nodes number

Nodes number /million	Nondimensional maximum Von Mises stress	Nondimensional maximum deformation
0.1	1.1011	0.9996
0.5	1.0067	0.9999
1	**1**	**1**
1.5	0.9991	1.0000

Note: Bold value indicates selected nodes number for stress simulation.

Table 12 Turbine performance

| Case	Total-to-static efficiency %
Fluid–thermal	
Without water-cooling	48.32
Water-cooling	45.57
Fluid–thermal–structural	
Without water-cooling	54.14
Water-cooling	50.76
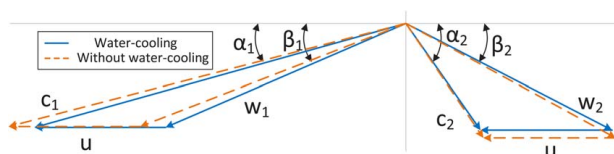
Fig. 12 Velocity triangle

s; without water-cooling: 1413.2 m/s) and relative velocity (water-cooling: 901.2 m/s; without water-cooling: 980.5 m/s) at the rotor inlet decrease. This implies that the liquid water in the front chamber prevents the gas discharge through the axial clearance. The increase in the area-average pressure at the nozzle outlet also confirms the phenomenon (water-cooling: 1.074 MPa; without water-cooling: 0.928 MPa). Besides, the liquid water entering the blade passage also reduces the absolute (water-cooling: 446.7 m/s; without water-cooling: 474.2 m/s) and relative velocity (water-cooling: 798.8 m/s; without water-cooling: 822.0 m/s) at the outlet.

To provide more detail, the single blade moment within one cycle is monitored (Fig. 13). The blade moment is calculated by integrating the moment throughout the entire blade height (from hub to tip). The center of the moment calculation is the origin of the coordinate system, and the direction is the same as the rotational direction. This can reflect the blade state at different positions compared to the whole moment. The initial position for the monitored blade is shown in Fig. 13(*a*), which is about to enter the working section. As shown in Fig. 13(*b*), a negative moment is observed when the rotor blade enters the working section. This is caused by the leakage flow at the axial clearance. As shown in Fig. 14, the velocity direction is opposite to the rotational direction at the leading edge of the blade. The liquid water retained in the passage is pushed onto the blade suction side (Fig. 14(*a*)), causing a higher reverse moment than without water-cooling (Fig. 13(*b*) 0–9.6 deg). As the blade rotates, the liquid water and gas retained in the passage are continuously discharged, and the blade moment gradually rises. Notably, the water-cooled moment is higher at 22–35 deg (see Fig. 13). One reason is the deformation. As shown in Fig. 15, the axial clearance without water-cooling is 1.97 mm, larger than the mean axial clearance of water-cooling (about 1 mm). The higher axial displacement for water-cooling causes a significant increase in the pressure value and distribution range at the pressure side. Besides, the separation vortices in the passage are evident without water-cooling, resulting in more flow losses (Fig. 14). In addition, the liquid water fills the axial front and tip clearance so that the leakage gas decreases while working gas increases (Fig. 16).

When the blade rotates to nozzle 2, the reverse moment is found again between 40 and 46 deg. The absolute value is much larger than the case without water-cooling (see Fig. 13(*b*)). As shown in Fig. 17, many swirls appear at the leading edge after water-cooling. Due to the axial deflection of the rotor, the gas leakage from the previous nozzle (nozzle 1) is hard to flow into the blade passage. The pressure at the pressure side is correspondingly lower than the suction side. Besides, the gap between the continuous nozzles also provides space for the radial movement of liquid water (see Fig. 17(*a*) vector). This also causes vortices at the bottom half of the passage (Fig. 17(*a*)). The moment then proceeds to increase. However, the peak moment decreases compared to the previous nozzle. The most liquid water flows through the blade passage at nozzle 1. During nozzle 2, the separation vortex appears (Fig. 18). Besides, as shown in Fig. 16, the mass fraction of the liquid water in the axial front and tip clearance also reduces, increasing the leakage gas. Subsequently, the moment tends to stabilize after nozzle 2. Figure 13(*b*) also shows that the minimum
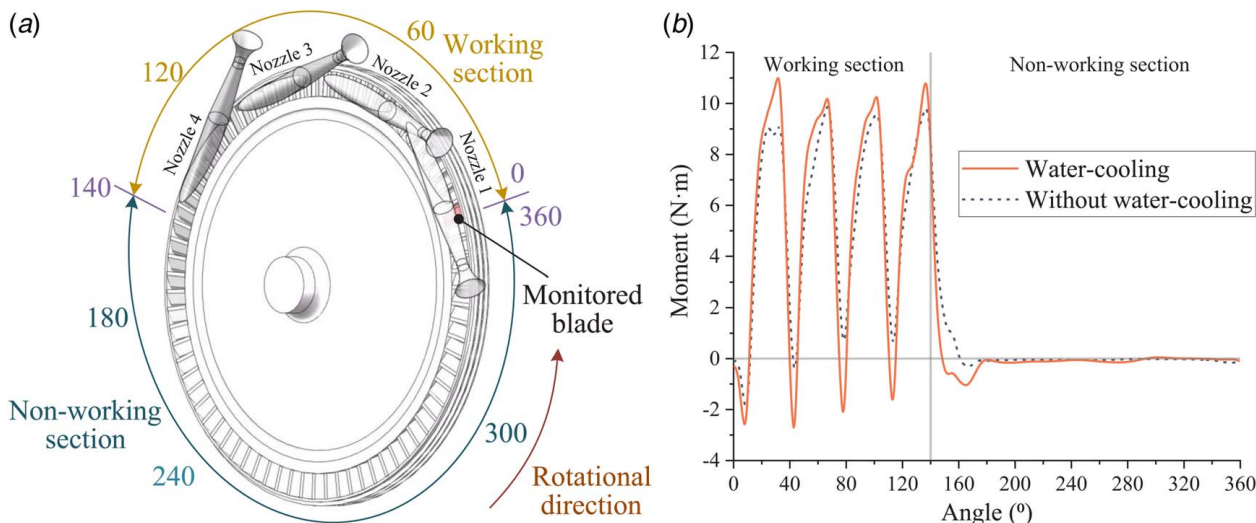
Fig. 13 Blade moment within one cycle: (*a*) position of monitored blade and (*b*) moment variation

Fig. 14 Velocity field and mass fraction of liquid water distribution at nozzle 1 (blade-to-blade rotor view at 50% blade span): (*a*) water-cooling and (*b*) without water-cooling

moment rises with the blade rotation, while for non-water-cooling, it stabilizes after nozzle 2. As shown in Fig. 17, the minimum value typically occurs just entering the nozzle. The mass fraction of liquid water at this location decreases from nozzle 1 to nozzle 4. Therefore, the working gas can enter the blade passages more efficiently, and the moment increases.

After the blade leaves the nozzle working section, the relative velocity of the leaking gas is opposite to the liquid water in the axial front clearance. The liquid water is then pushed into the blade passage, as shown in Fig. 19(*a*). Besides, the radial and tangential velocity in Fig. 19(*b*) accelerate and change the direction of the liquid water. This results in a faster decrease of blade moment compared without water-cooling when entering the nonworking section (Fig. 13(*b*)). The leaked gas velocity from nozzle 4 is constantly decreasing (Fig. 19). When the relative velocity of the leaking gas cannot accelerate the liquid water, the liquid water is

Fig. 15 Pressure distribution on the turbine pressure side at 28.8 deg: (*a*) water-cooling and (*b*) without water-cooling

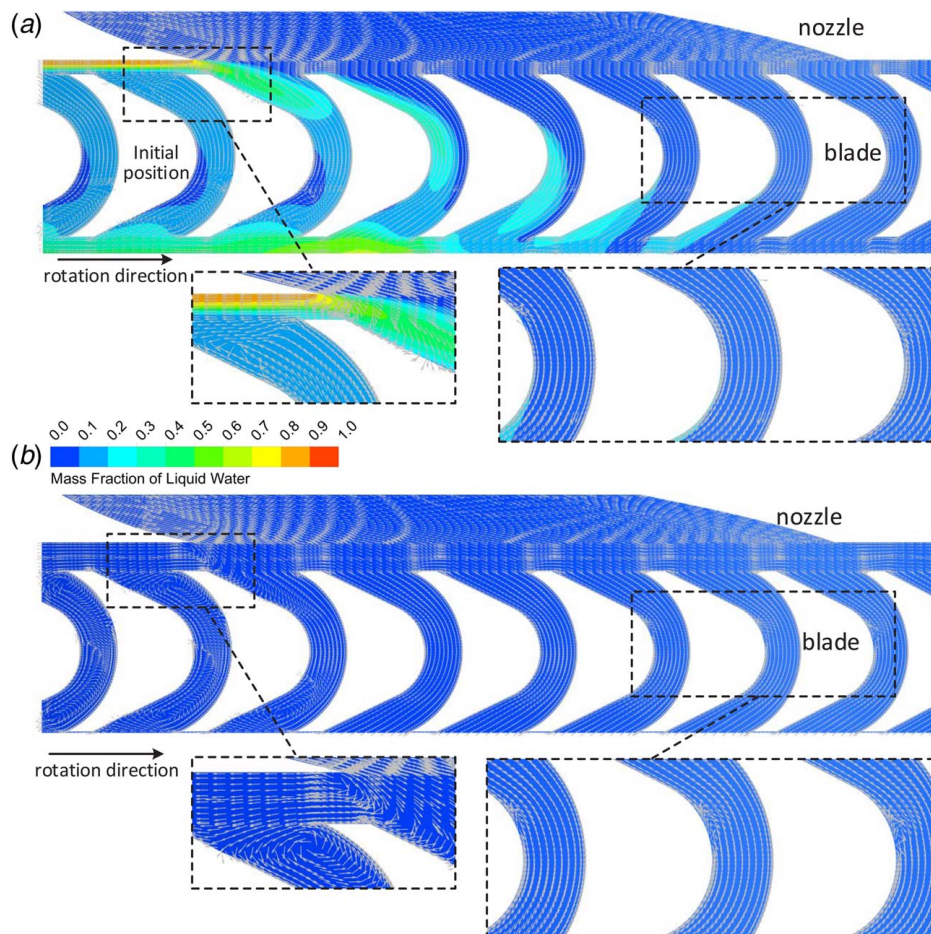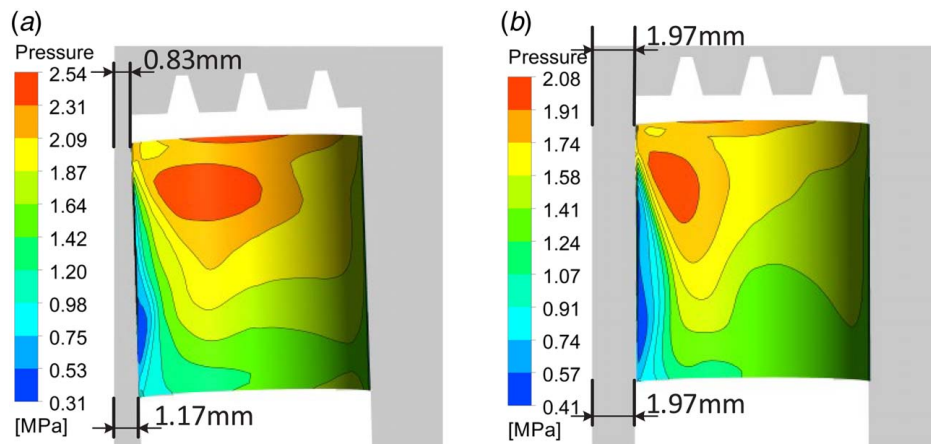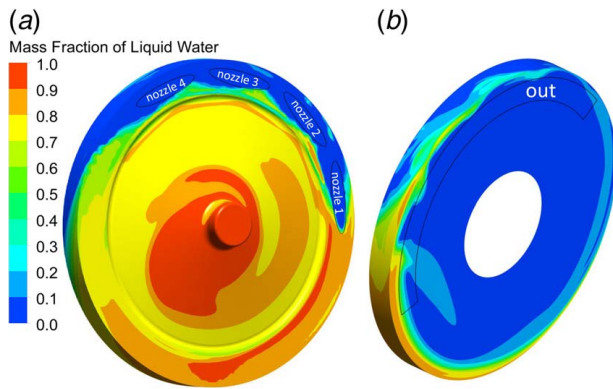**Fig. 16 The mass fraction of liquid water within the fluid domain: (a) front and (b) back**

Fig. 18 Velocity field and mass fraction of liquid water distribution at nozzle 2 (blade-to-blade rotor view at 50% blade span)

pushed by the blades subsequently. Thus, the blade moment becomes negative again, starting from about 148 deg (Fig. 13(*b*)). The velocity of the gas–water mixture in the blade passage progressively reaches the rotational speed. The mass fraction of liquid water distribution tends to stabilize due to the lack of more driving force. Therefore, the negative moment rises slightly after 167 deg and reaches stability at about 180 deg. In addition, the liquid water in the nonworking section also enters the tip clearance, as shown in Fig. 16(*a*). The liquid water accumulates as the rotor rotates, and the high-speed gas leaking into the tip clearance carries it out in the working section (Fig. 16(*b*)).

The temperature distributions for the turbines with and without water-cooling are depicted in Fig. 20. The wall temperatures are smeared circumferentially due to the high-speed rotor rotation. After the water-cooling, there is a significant temperature decrease on the front surface of the wheel, and the area-average temperature drops from the original 1117 K to 378 K. As shown in Fig. 21, the temperature increase in the radial direction is due to the working gas leakage. The large temperature gradient near the blade during water-

cooling is due to the high gas–liquid mixing phenomenon. Near the wheel center, the temperature changes slightly because most of the liquid water is attached to the wheel. The area-average wall temperature at the tip clearance side is also decreased (water-cooling: 761 K; without water-cooling: 1185 K). As illustrated in Figs. 16 and 21, the liquid water can enter the tip clearance. However, it is discharged by the high-speed working gas during the working section (Fig. 16). Also, the liquid water is mainly located at the turbine casing due to the centrifugal velocity, resulting in less water distribution at the grooves of rotor clearance. Therefore, the temperature reduction is lower than that on the front side. For the back side, the area-average wall temperature decreases from 1136 K to 743 K. Besides, the fluid temperature is higher than the solid wall temperature (see Fig. 21). Therefore, the heat generated
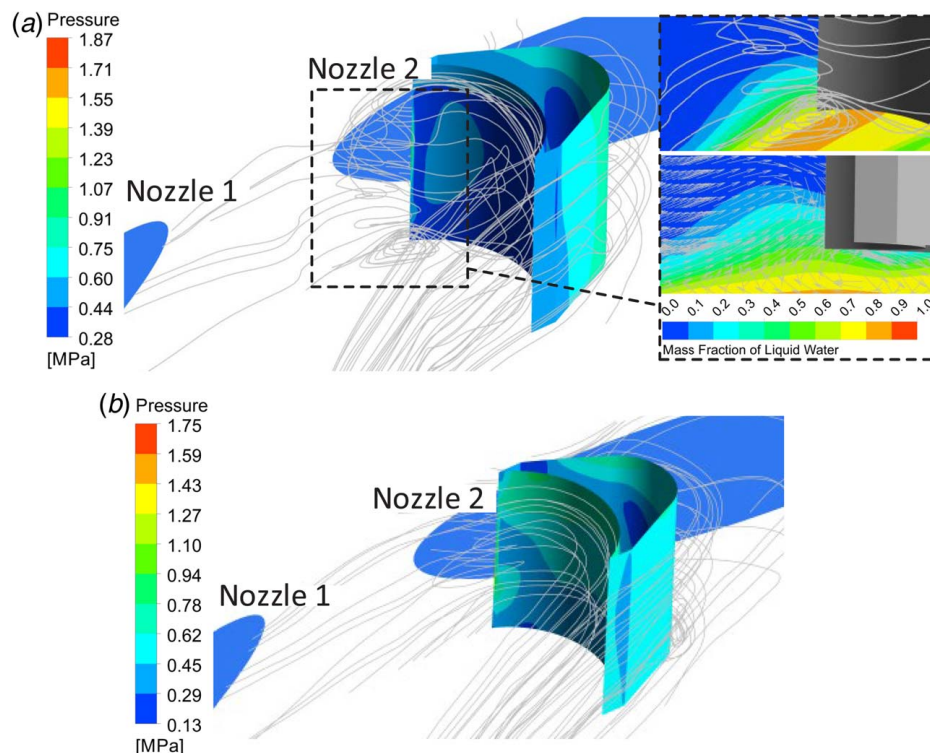
Fig. 17 Flow characteristic at 43.2 deg: (a) water-cooling and (b) without water-cooling

(a) nozzle 4

rotation direction

0.0 0.1 0.2 0.3 0.4 0.5 0.6 0.7 0.8 0.9 1.0
Mass Fraction of Liquid Water

(b) nozzle 4

rotation direction

0.0 0.1 0.2 0.3 0.4 0.5 0.6 0.7 0.8 0.9 1.0
Mass Fraction of Liquid Water
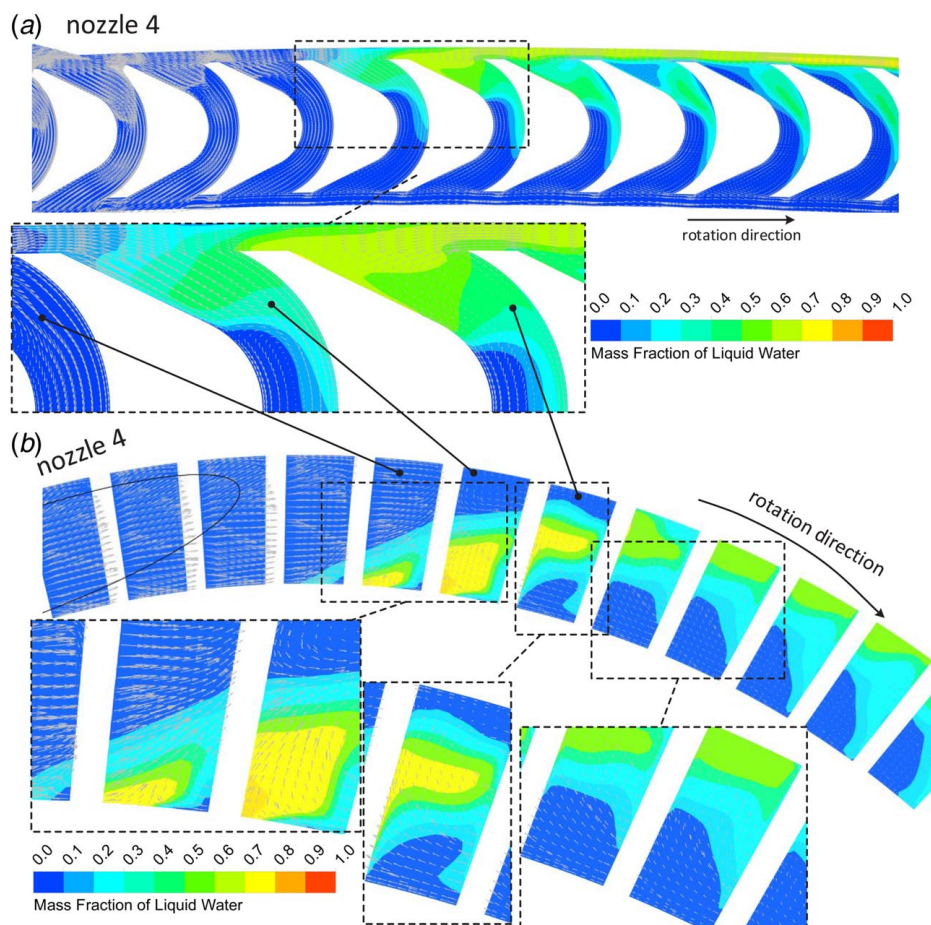
Fig. 19 Velocity field and mass fraction of liquid water distribution after nozzle 4 (the arrow size corresponds to the relative velocity): (a) 50% span and (b) blade inlet

(a)
Temperature
993
926
860
793
726
660
593
526
460
393
326
[K]

front   back

(b)
Temperature
1213
1126
1039
952
864
777
690
602
515
428
341
[K]

front   back
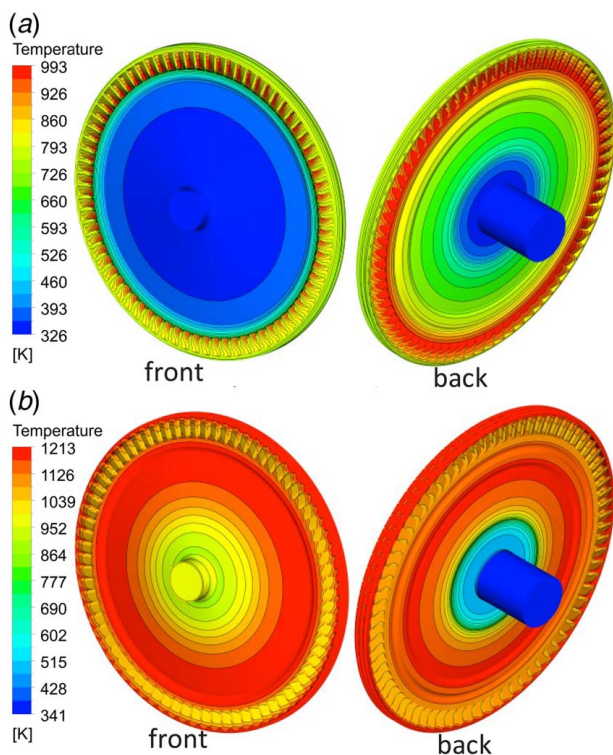
Fig. 20 Rotor wall temperature distribution: (a) water-cooling and (b) without water-cooling

on the backside is mainly carried away from the solid thermal conduction.

4.3 Stress and Deformation Analysis. Since material properties are involved with nonlinear problems, the present section first explores the effect of the loading order on stress. The stress and deformation distributions before and after cooling are then

Temperature
1022
994
966
938
910
882
854
826
798
770
742
[K]

working section
non-working section

axis

0.0 0.1 0.2 0.3 0.4 0.5 0.6 0.7 0.8 0.9 1.0
Mass Fraction of Liquid Water

Fig. 21 Velocity field and mass fraction of liquid water distribution parallel to the rotational axis (the arrow size corresponds to the relative velocity)

Table 13 Loads for mechanical stress

Load	Pressure	Rotation
Case 1	–	√
Case 2	√	–
Case 3	First	Second
Case 4	Second	First
Case 5	At the same time	

compared. Because the time constant in the heat conduction is significantly larger than the mechanical force, the influence of aerodynamic and centrifugal forces at zero-thermal-strain reference temperatures is first considered in Table 13. Figure 22 shows the results of nondimensional Von Mises stress due to aerodynamic and centrifugal forces, and the yield strength at the ambient temperature is used as the dimensionless reference value. The material has entered the plastic section from the maximum value of case 1, referring to Fig. 9. The aerodynamic force, however, remains in the elastic section since the aerodynamic force is relatively small compared to the centrifugal force. Through different loading orders, the stress values and the locations of the maximum value are almost the same for cases 3 and 5. However, if the centrifugal force is applied first and the aerodynamic force is then loaded, the position of the maximum value changes and the stress value decreases. At this point, the centrifugal force first leads the material into the plastic section, causing the material to soften. Then, a small force is applied to produce a more obvious strain. Therefore, different loading orders can influence the results. For mechanical stress, how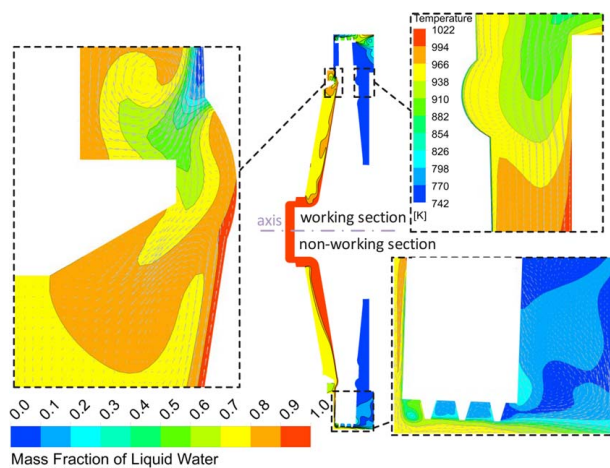ever, no significant difference occurs. This also indicates that aerodynamic force has little effect on mechanical stress.

Next, the temperature effect on stress is further studied. Table 14 provides the loading orders for the different cases. As shown in

Fig. 23(a), the material enters the plastic section, referring to Fig. 9. The centrifugal force and temperature are the interactions between the two large forces. In addition, temperature changes Young's modulus and yield strength, which further changes the stress distribution. Thus, substantial changes in the stress distribution are observed at the blade from Cases 7 and 8. Comparing Cases 7 and 9, the difference in stress distribution appears slight, while the difference only occurs at the transition of the blade root. By combining Figs. 22 and 23, the loading order is concluded to produce effects on the stress results. Therefore, it is necessary to consider the actual operating condition of the turbine. This paper recommends using the order of aerodynamic force, centrifugal force, and temperature to calculate stress distribution.

Figure 24 shows the results considering all three loads. Comparing Fig. 24(b), Fig. 20, and Fig. 9, it is clear that the root of the wheel and blade without water-cooling has reached fracture strength. After water-cooling, the temperature gradient at the wheel center decreases significantly, reducing the stress at the root of the wheel. However, the increased temperature gradient at the blade raises the stress. Due to the reduced temperature, the strength is consequently increased, allowing stress within the plastic section. This is similarly reflected in the size of the plastic zone. Figure 25 shows that the plastic zone at the wheel disappears extensively after water-cooling, while it arises at the blade instead.

Figure 26 shows the corresponding displacement distributions. The total displacement becomes larger after water-cooling (water-cooling: 1.34 mm; without water-cooling: 1.24 mm), and the displacement of the back side is higher than that of the front side. The axial displacement produced by water-cooling is more significant and increases with the radius (maximum: 1.24 mm; minimum: −0.04 mm). In contrast, the axial displacement without water-cooling expands to both sides slightly and almost uniformly (maximum: 0.12 mm; minimum: −0.13 mm). In the radial direction, the displacement without water-cooling (1.23 mm) is larger
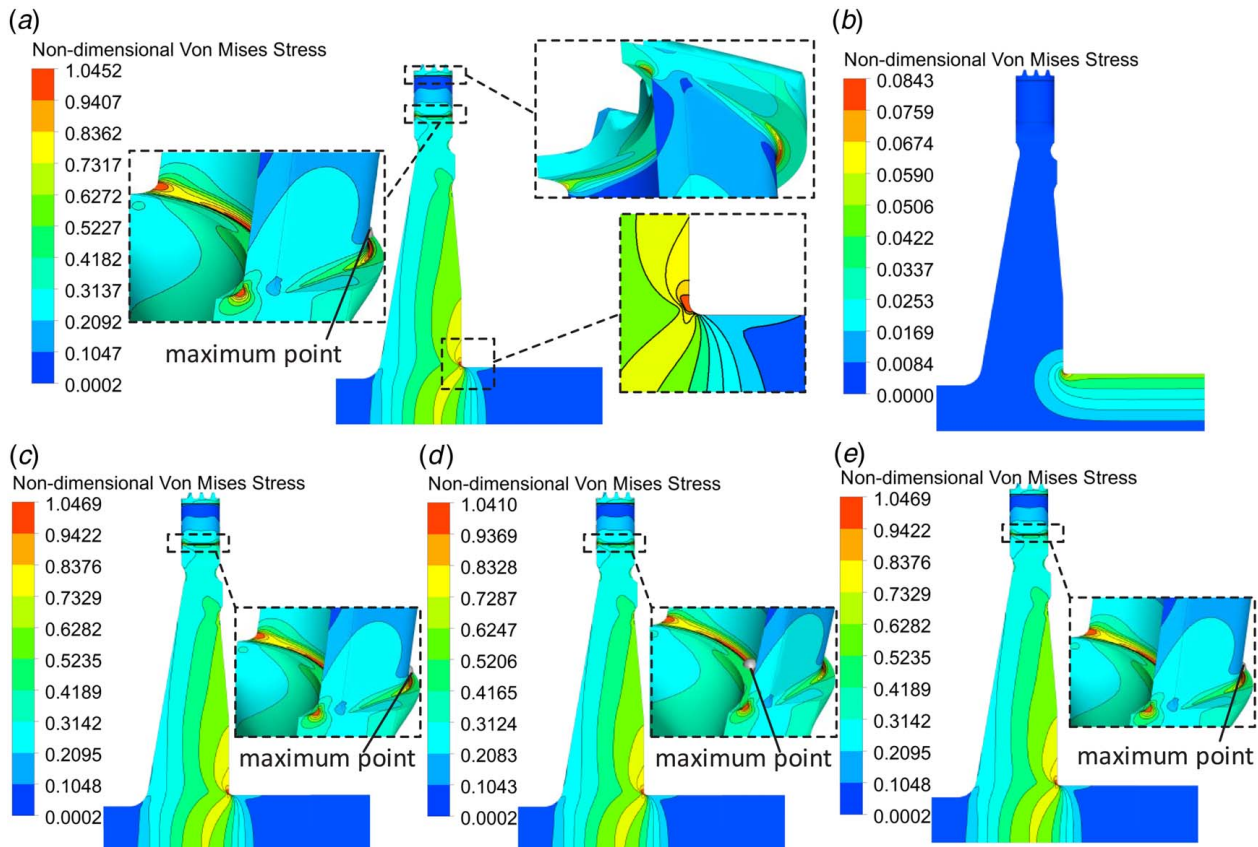
Fig. 22 Nondimensional Von Mises stress for mechanical stress: (a) case 1, (b) case 2, (c) case 3, (d) case 4, and (e) case 5

Table 14 Loads considering the temperature effect

Load	Rotation	Temperature
Case 6	–	√
Case 7	First	Second
Case 8	Second	First
Case 9	At the same time	

than water-cooling (0.64 mm). In addition, the distribution without water-cooling is almost entirely elongated gradually along the radial direction. In contrast, the radial displacement on the front side is significantly lower than on the back side after water-cooling. The main reason is due to the difference in the temperature distribution. A more uniform temperature distribution without water-cooling leads to a minor temperature gradient. However, the front surface temperature drops sharply when water-cooled, thus causing a
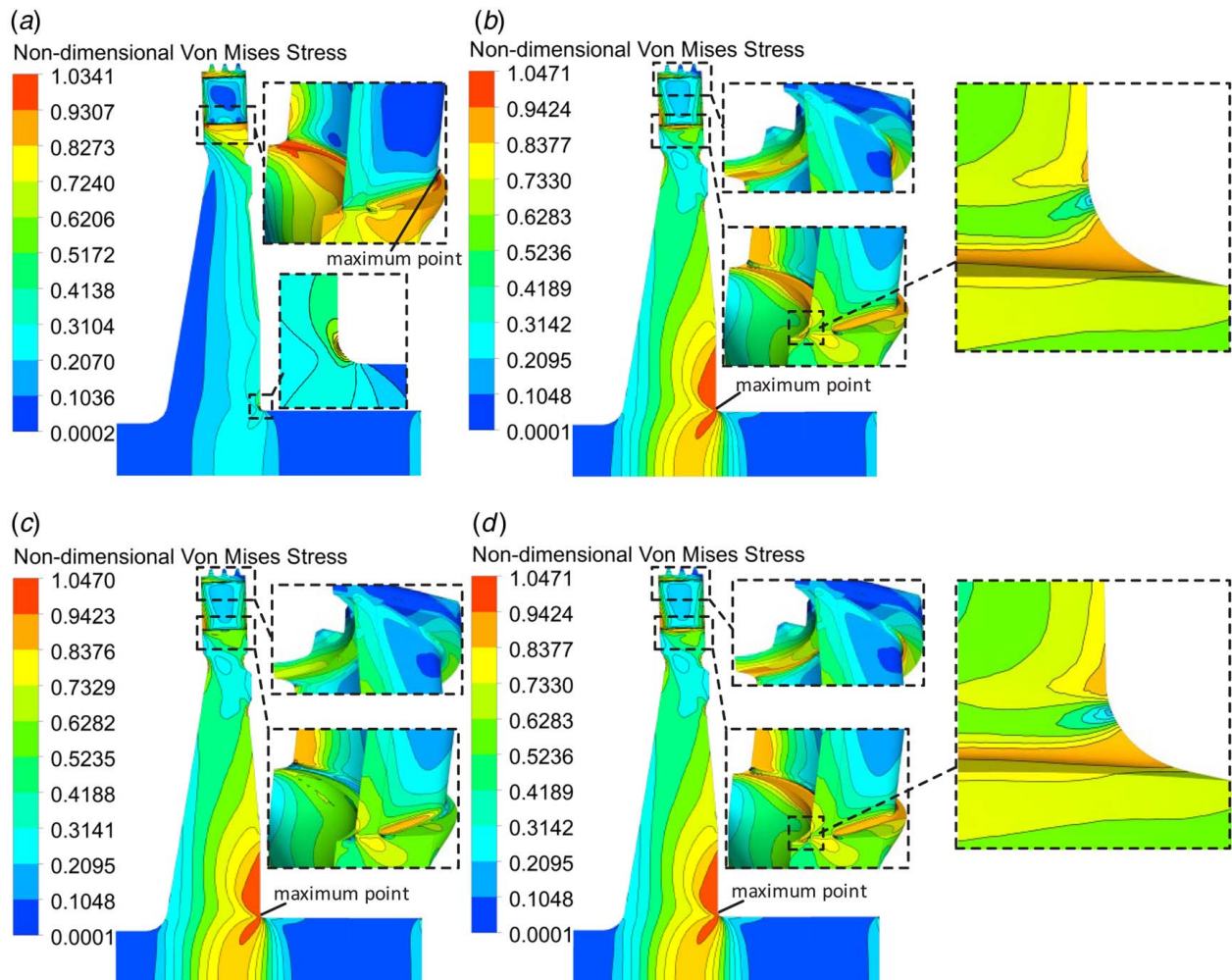
Fig. 23 Nondimensional Von Mises stress considering temperature effect: (*a*) case 6, (*b*) case 7, (*c*) case 8, and (*d*) case 9
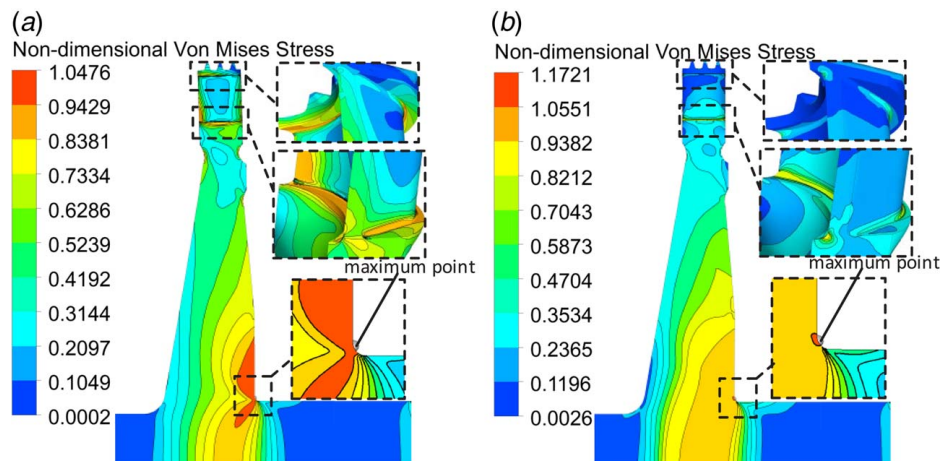
Fig. 24 Nondimensional Von Mises stress considering whole loads: (*a*) water-cooling and (*b*) without water-cooling
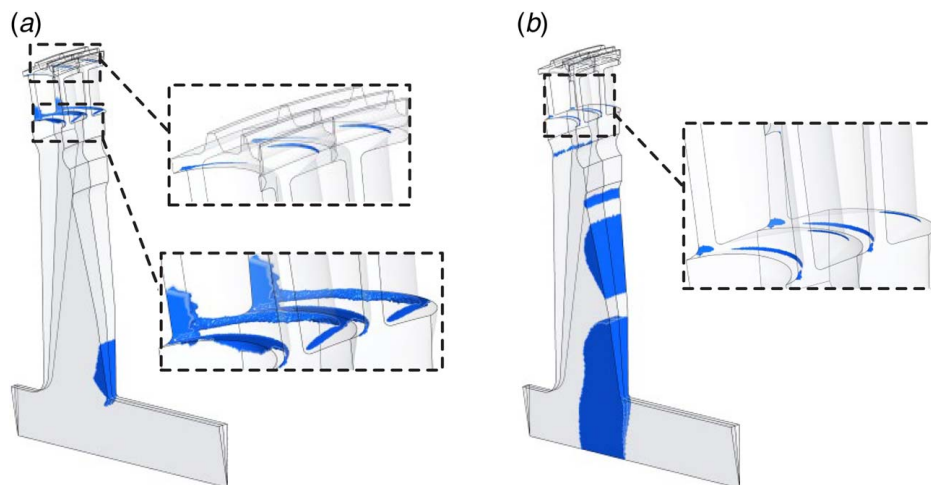
Fig. 25 Plastic zone considering whole loads: (*a*) water-cooling and (*b*) without water-cooling
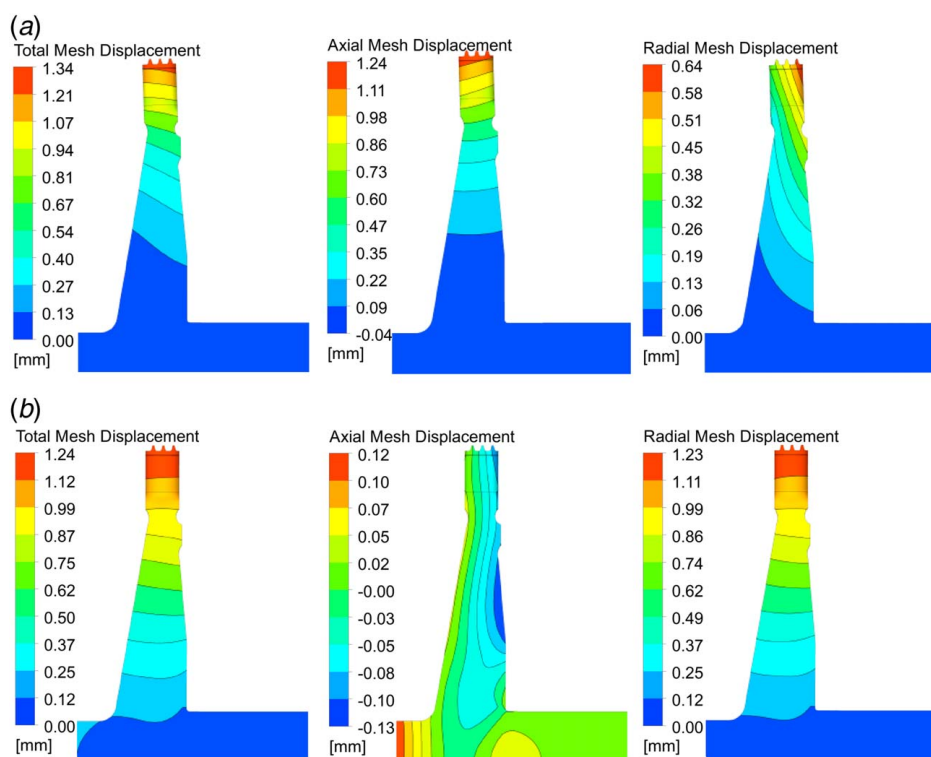
Fig. 26 Distribution of mesh displacement: (*a*) water-cooling and (*b*) without water-cooling

decrease in Young's modulus, thermal expansion coefficient, and elongation. Therefore, a significant blade tilt occurs after water-cooling.

5 Conclusion and Future Work

This paper proposes a numerical method for the fluid–thermal–structural simulation of partial admission axial impulse turbines with liquid jet impingement cooling used in underwater vehicles. Detailed computational methods in different solvers and their coupling procedures are presented with validation cases. The computational model is further used to study the flow, heat, and stress characteristics for water-cooling of axial direction compared with non-water-cooling. Key findings are the following:

(1) The deformation has a significant effect on turbine efficiency. The consideration of deformation can result in a relative difference of 10%. Therefore, the fluid–thermal–structural coupling method is needed to obtain the deformation. In addition, water-cooling causes an efficiency loss of 3.38% since the liquid water directly affects the velocity at the rotor inlet and outlet.
(2) The liquid water is discharged from the rotor passage through the high-speed working gas in the working section. In the nonworking section, it mainly exists in the axial front clearance attached to the wheel. Besides, there is also a large amount of liquid water in the tip clearance, while the distribution is near the turbine casing. In addition, little liquid water fills in the axial back clearance. This directly affects the temperature distributions of the rotor.

(3) The nonlinear problem for different loading orders has inconsistent stress results. Therefore, a reasonable loading order of aerodynamic force, centrifugal force, and temperature is recommended regarding the actual working process of the turbine. By comparing the stress with and without water-cooling, the plastic zones and stress are reduced for the wheel, allowing most of the region within yield strength. However, it is increased for the blade, but the temperature decrease improves the material strength and avoids damage. Therefore, water-cooling can ensure stable turbine operation due to the slight total deformation.

Future work will further study the loss characteristics under axial water injection cooling.

Acknowledgment

Funding Data

Conflict of Interest

There are no conflicts of interest.

Data Availability Statement

The datasets generated and supporting the findings of this article are obtainable from the corresponding author upon reasonable request.

Nomenclature

c = factor in Lee model
h = convective heat transfer coefficient, $W/(m^2 \cdot K)$
k = kinetic energy per unit mass, J/kg
p = pressure, Pa
q = heat flux, W/m^2
t = time, s
$\mathbf{v}$ = vector of velocity, m/s
E = total energy, J
F = body force, N
M = moment, $N \cdot m$
P = power, W
S = factor in turbulence model
T = temperature, K
$\dot{m}$ = mass flowrate, kg/s
h_i = sensible enthalpy for species i, J/kg
h_{lh} = latent heat, J/kg
k_{eff} = effective conductivity, $W/(m \cdot K)$
k_T = thermal conductivity, $W/(m \cdot K)$
$\mathbf{J}_i$ = diffusion flux of species i, $kg/(m^2 \cdot s)$
G_k = production rate of turbulence, $kg/(m \cdot s^3)$
S_h = energy source, W/m^3
Y_i = mass fraction for species i
C_1, C_2 = factor in turbulence model
S_l, S_{mf} = mass source, $kg/(m^3 \cdot s)$
Δh_{is} = ideal enthalpy drop, J/kg

Greek Symbols

α = volume fraction
β = relaxation factor
ε = turbulent dissipation rate, m^2/s^3
η = efficiency

μ_m, μ_t = molecular viscosity; turbulent viscosity, $Pa \cdot s$
ρ = density, kg/m^3
$\sigma_k, \sigma_\varepsilon$ = turbulent Prandtl numbers for k and ε
σ = stress, Pa
$\bar{\bar{\tau}}, \bar{\bar{\tau}}_{eff}$ = stress tensor; effective stress tensor, Pa
ν = kinematic viscosity, m^2/s
ω = rotational speed, rad/s

Subscripts

l = liquid
m = mean
s = solid
w = wall
F = fluid
lv = liquid to vapor
mf = mix-fluid
sat = saturation
ts = total-to-static
vl = vapor to liquid

Superscript

k = index of iteration loop

References

[1] Moustapha, H., Zelesky, M. F., Baines, N. C., and Japikse, D., 2003, *Axial and Radial Turbines*, Concepts NREC Press, White River Junction, VT.

[2] Zhengping, Z., Songtao, W., Huoxing, L., and Weihao, Z., 2018, *Axial Turbine Aerodynamics for Aero-Engines: Flow Analysis and Aerodynamics Design*, Springer Press, Singapore.

[3] Zhou, Z., Li, H., Xie, G., and You, R., 2020, "Film Cooling Performance on Turbine Blade Suction Side With Various Film Cooling Hole Arrangements," Proceedings of the ASME Turbo Expo 2020: Power for Land, Sea, and Air, ASME Paper No. GT2020-14836.

[4] Han, J. C., Dutta, S., Ekkad, S., and Dutta, S., 2013, *Gas Turbine Heat Transfer and Cooling Technology*, CRC Press, Boca Raton, FL.

[5] Bunker, R. S., 2017, "Evolution of Turbine Cooling," Proceedings of ASME Turbo Expo 2017: Turbomachinery Technical Conference and Exposition, ASME Paper No. GT2017-63205.

[6] Zheng, Z., Shi, X., Yi, Y., and Shi, H., 2006, "Development and Application of Gas Turbine to Torpedo Power," Torpedo Technol., **14**(4), pp. 11–15.

[7] Kiely, D. H., and Moore, J. T., 2002, "Hydrocarbon Fueled UUV Power Systems," Proceedings of the 2002 Workshop on Autonomous Underwater Vehicles, San Antonio, TX, June 20–21, pp. 121–128.

[8] Qin, K., Wang, H., Wang, X., Sun, Y., and Luo, K., 2020, "Thermodynamic and Experimental Investigation of a Metal Fuelled Steam Rankine Cycle for Unmanned Underwater Vehicles," Energy Convers. Manage., **223**, p. 113281.

[9] Qin, K., Wang, H., Qi, J., Sun, J., and Luo, K., 2022, "Aerodynamic Design and Experimental Validation of High Pressure Ratio Partial Admission Axial Impulse Turbines for Unmanned Underwater Vehicles," Energy, **239**, p. 122242.

[10] Wang, H., Luo, K., Yang, Q., Huang, C., and Qin, K. A., 2021, "Fluid-Thermal Analysis of Partial Admission Axial Turbines," Proceedings of the Global Power and Propulsion Society, Xi'an, Shaanxi, China, Paper No. GPPS-TC-2021-0105.

[11] Fraas, A. P. (1980). "Summary of Research and Development Effort on Air and Water Cooling of Gas Turbine Blades," Oak Ridge National Lab., Technical Report No. ORNL/TM-6254.

[12] Bayley, F. J., and Martin, B. W., 1970, "A Review of Liquid Cooling of High-Temperature Gas-Turbine Rotor Blades," Proc. Inst. Mech. Eng., **185**(1), pp. 219–227.

[13] Fossen, G., and Stepka, F. S. (1979). "Review and Status of Liquid-Cooling Technology for Gas Turbines," NASA Lewis Research Center, Technical Report No. 19790014256.

[14] Horner, M. W., Cincotta, G. A., and Caruvana, A., 1981, "Test Verification of Water Cooled Gas Turbine Technology," Proceedings of the ASME Turbo Expo 1981: Power for Land, Sea, and Air, ASME Paper No. 81-GT-66.

[15] Schilke, P. W., and DeGeorge, C. L., 1982, "Water-Cooled Gas Turbine Monometallic Nozzle Fabrication and Testing," ASME J. Eng. Power, **104**(3), pp. 607–616.

[16] Amano, R. S., 1982, "Numerical Study of Liquid Cooling Gas Turbine Blade," Proceedings of the ASME Turbo Expo 1982: Power for Land, Sea, and Air, ASME Paper No. 82-GT-116.

[17] Ladisch, H., Schulz, A., and Bauer, H. R., 2009, "Heat Transfer Measurements on a Turbine Airfoil With Pressure Side Separation," Proceedings of the ASME Turbo Expo 2009: Power for Land, Sea, and Air, ASME Paper No. GT2009-59904.

[18] Duchaine, F., Maheu, N., Moureau, V., Balarac, G., and Moreau, S., 2013, "Large-Eddy Simulation and Conjugate Heat Transfer Around a Low-Mach Turbine Blade," ASME J. Turbomach., **136**(5), p. 051015.

[19] Lorenz, M., Schulz, A., and Bauer, H. J., 2011, "Experimental Study of Surface Roughness Effects on a Turbine Airfoil in a Linear Cascade—Part I: External Heat Transfer," ASME J. Turbomach., **134**(4), p. 041006.

[20] Elhabeshi, N. I., and Guo, S. M., 2005, "The Experimental and Computational Study of a New Cooling Strategy for Turbomachinery Rotational Components," Proceedings of the ASME Turbo Expo 2005: Power for Land, Sea, and Air, ASME Paper No. GT2005-68660.

[21] Townsend, J., Kerrebrock, J., and Stickler, D., 2008, "Experimental Evaluation of a Turbine Blade With Potassium Evaporative Cooling," J. Propul. Power, **24**(3), pp. 410–415.

[22] Lytvynenko, O., Tarasov, O., Mykhailova, I., and Avdieieva, O., 2020, "Possibility of Using Liquid-Metals for Gas Turbine Cooling System," Proceedings of the 3rd International Conference on Design, Simulation, Manufacturing: The Innovation Exchange, Kharkiv, Ukraine, June 9–12, pp. 312–321.

[23] Zhang, Y., Cao, Y., Feng, Y., Li, D., and Qin, J., 2021, "Numerical Simulation of Convective Heat Transfer for an Internally Cooled Gas Turbine Using Liquid Metal," Int. J. Therm. Sci., **171**, p. 107230.

[24] Nirmalan, N. V., Weaver, J. A., and Hylton, L. D., 1998, "An Experimental Study of Turbine Vane Heat Transfer With Water–Air Cooling," ASME J. Turbomach., **120**(1), pp. 50–60.

[25] Ragab, R., and Wang, T., 2018, "An Experimental Study of Mist/Air Film Cooling With Fan-Shaped Holes on an Extended Flat Plate—Part 1: Heat Transfer," ASME J. Heat Transfer-Trans. ASME, **140**(4), p. 042201.

[26] Ragab, R., and Wang, T., 2018, "An Experimental Study of Mist/Air Film Cooling With Fan-Shaped Holes on an Extended Flat Plate—Part II: Two-Phase Flow Measurements and Droplet Dynamics," ASME J. Heat Transfer-Trans. ASME, **140**(4), p. 042202 .

[27] Wang, T., and Ragab, R., 2019, "Investigation of Applicability of Transporting Water Mist for Cooling Turbine Blades," ASME J. Therm. Sci. Eng. Appl., **12**(1), p. 011009 .

[28] Wang, T., and Abdelmaksoud, R., 2021, "Interactions of Wakes and Shock Waves With Two-Phase Air/Mist Cooling in a Transonic Gas Turbine Stage," Int. J. Heat Mass Transfer, **179**, p. 121652.

[29] Abdelmaksoud, R., and Wang, T., 2021, "A Numerical Investigation of Air/Mist Cooling Through a Conjugate, Rotating 3D Gas Turbine Blade With Internal, External, and Tip Cooling," ASME J. Therm. Sci. Eng. Appl., **13**(2), p. 021004 .

[30] Abdelmaksoud, R., Wang, T., and Zhao, L., 2022, "Validation of a Two-Phase CFD Model Air/Mist Film Cooling With Experimental Details—Part II: CFD Model Validation," ASME J. Therm. Sci. Eng. Appl., **14**(11), p. 111010.

[31] Cao, J., Ye, M., Li, H., Wang, T., and Che, Z., 2022, "Heat Transfer Enhancement by Mist/air Two-Phase Flow in a High-Temperature Channel," Int. J. Heat Mass Transfer, **193**, p. 122966.

[32] Feistel, R., 2018, "Thermodynamic Properties of Seawater, Ice and Humid Air: TEOS-10, Before and Beyond," Ocean Sci., **14**(3), pp. 471–502.

[33] Nayar, K. G., Sharqawy, M. H., Banchik, L. D., and Lienhard V, J. H., 2016, "Thermophysical Properties of Seawater: A Review and New Correlations That Include Pressure Dependence," Desalination, **390**, pp. 1–24.

[34] ANSYS, 2017, *ANSYS User's Guide Releases 18.2*, ANSYS Inc., Concord, MA.

[35] Antoine, C., 1888, "Vapor Pressure: A New Relationship Between Pressure and Temperature," CR Acad. Sci., **107**, pp. 681–685.

[36] Lemmon, E. W., Bell, I. H., Huber, M. L., and McLinden, M. O., 2010, *NIST Standard Reference Database 23: Reference Fluid Thermodynamic and Transport Properties-REFPROP, Version 9.0, National Institute of Standards and Technology*, Standard Reference Data Program, Gaithersburg.

[37] Aissa, M., Verstraete, T., and Vuik, C., 2017, "Toward a GPU-Aware Comparison of Explicit and Implicit CFD Simulations on Structured Meshes," Comput. Math. Appl., **74**(1), pp. 201–217.

[38] Cavalca, D. F., Bringhenti, C., Campos, G. B., Tomita, J. T., and Silva, O. F. R., 2018, "Development and Convergence Analysis of an Effective and Robust Implicit Euler Solver for 3D Unstructured Grids," J. Comput. Phys., **367**, pp. 399–415.

[39] Back, L. H., Massier, P. F., and Gier, H. L., 1964, "Convective Heat Transfer in a Convergent-Divergent Nozzle," Int. J. Heat Mass Transfer, **7**(5), pp. 549–568.

[40] DeLise, J. C., and Naraghi, M., 1995, "Comparative Studies of Convective Heat Transfer Models for Rocket Engines," 31st Joint Propulsion Conference and Exhibit, San Diego, CA, June 10–12, Paper No. AIAA-95-2499.

[41] Marineau, E. C., Schetz, J. A., and Neel, R. E., 2007, "Turbulent Navier-Stokes Simulations of Heat Transfer With Complex Wall Temperature Variations," J. Thermophys. Heat Transfer, **21**(3), pp. 525–535.

[42] Yi, J., Yanli, M., Weichen, W., and Liwu, S., 2010, "Inhibition Effect of Water Injection on Afterburning of Rocket Motor Exhaust Plume," Chin. J. Aeronaut., **23**(6), pp. 653–659.

[43] Yu, S., 2015, "Simulation and Experiment Research on Temperature Reduction of Rocket Engine Jet by Water Injection," Ph.D. thesis, Beijing institute of Technology, Beijing, China.